

Optical-Resolution Photoacoustic Microscopy: Auscultation of Biological Systems at the Cellular Level

Song Hu^{†‡} and Lihong V. Wang^{†*}

[†]Optical Imaging Laboratory, Department of Biomedical Engineering, Washington University in St. Louis, St. Louis, Missouri; and [‡]Department of Biomedical Engineering, University of Virginia, Charlottesville, Virginia

ABSTRACT Photoacoustic microscopy (PAM) offers unprecedented sensitivity to optical absorption and opens a new window to study biological systems at multiple length- and timescales. In particular, optical-resolution PAM (OR-PAM) has pushed the technical envelope to submicron length scales and millisecond timescales. Here, we review the state of the art of OR-PAM in biophysical research. With properly chosen optical wavelengths, OR-PAM can spectrally differentiate a variety of endogenous and exogenous chromophores, unveiling the anatomical, functional, metabolic, and molecular information of biological systems. Newly uncovered contrast mechanisms of linear dichroism and Förster resonance energy transfer further distinguish OR-PAM. Integrating multiple contrasts and advanced scanning mechanisms has capacitated OR-PAM to comprehensively interrogate biological systems at the cellular level in real time. Two future directions are discussed, where OR-PAM holds the potential to translate basic biophysical research into clinical healthcare.

INTRODUCTION

Optical microscopy, capable of identifying cellular and sub-cellular structures based on their unique spectral signatures, has long been a driving force in modern biophysics research. Linear (1) and nonlinear (2) fluorescence microscopy have served as technical mainstays for decades. Elastic (3,4) and inelastic (5) scattering microscopy are also well established. In contrast, the development of *in vivo* optical absorption microscopy lags behind.

The invention of optical-resolution photoacoustic microscopy (OR-PAM) has narrowed the gap, by enabling acoustic detection of thermoelastically induced pressure waves from biomolecules' absorption of short-pulsed or intensity-modulated light (6). Within only a few years, OR-PAM has successfully demonstrated a wide variety of absorption-based anatomical (7), functional (8,9), metabolic (10,11), molecular (12), and genetic (13) contrasts, and has found broad applications in neurology (14), vascular biology (15,16), dermatology (17), ophthalmology (18,19), and tissue engineering (20).

Photoacoustic tomography, with unique spatial capability, maintains high spatial resolution across four major length scales in biology: organelle, cell, tissue, and organ (Fig. 1 A) (21). At the cellular level, optical focusing offers OR-PAM with 2.6- μm lateral resolution, whereas optical diffusion limits its imaging depth to 1.2 mm in biological tissues (22). The optically defined lateral resolution can be scaled down to submicron (500 nm) (23) or even subwavelength (200 nm) (24) to image organelle structures, at the expense of imaging depth. In contrast, the imaging depth of photoacoustic microscopy (PAM) can be scaled up to a few milli-

meters with an acoustically defined lateral resolution. Such an implementation is well known as acoustic-resolution PAM, which breaks through the optical diffusion limit (25). Although the lateral resolution can be scaled between the optical and acoustic regimes, the axial resolution (typically 15 μm) is codetermined acoustically by the bandwidths of both the received photoacoustic signal and the ultrasonic detector.

Instrumentation

In a typical OR-PAM design (Fig. 1 B), the diffraction-limited optical focus is achieved by a microscope objective. To spatially separate the coaxially aligned optical excitation and acoustic detection, an optical-acoustic beam combiner with a glass-oil interface is positioned beneath the objective. A decent match in optical refractive index at the interface ensures optical transparency, whereas a significant mismatch in acoustic impedance provides acoustic reflection. To improve the sensitivity of acoustic detection, a concave acoustic lens is ground into the rhomboid prism of the beam combiner. Although confocally aligned with the optical focus, the acoustic focus ($\sim 50 \mu\text{m}$ in diameter) is 20 times coarser than its optical counterpart due to the much longer acoustic wavelength. A portion of the generated spherical acoustic wave is converted into a plane wave by the acoustic lens and received by an unfocused ultrasonic transducer after being reflected twice at the inclined surfaces of the rhomboid prism. The second acoustic reflection is crucial to achieve high detection sensitivity, because it regains the longitudinal wave that was converted into the shear wave at the solid-oil interface (22,26,27). A correction lens is attached to the right-angle prism of the beam combiner to compensate for the optical aberrations along the light path.

Submitted November 1, 2012, and accepted for publication July 12, 2013.

*Correspondence: lhwang@wustl.edu

Editor: Brian Salzberg.

© 2013 by the Biophysical Society
0006-3495/13/08/0841/7 \$2.00



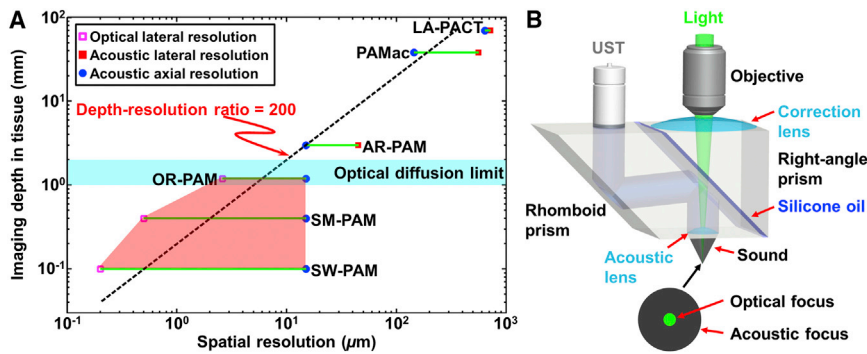


FIGURE 1 (A) Multiscale photoacoustic tomography. SW, subwavelength; SM, submicron; AR, acoustic resolution; PAMac, photoacoustic macroscopy; LA, linear array; PACT, photoacoustic computed tomography. The pentagon zone indicates the OR-PAM regime. (B) Schematic of OR-PAM. UST, ultrasonic transducer. Reproduced from Wang and Hu (21).

MAJOR ENDOGENOUS CONTRASTS

Capitalizing on the narrow nonionizing optical band of the electromagnetic spectrum, OR-PAM can identify a variety of endogenous chromophores through their unique absorption spectra (Fig. 2 A). In the ultraviolet region, DNA and RNA show strong absorption and have been used for imaging of cell nuclei (Fig. 2 B), which enables noninvasive in vivo label-free histology (7). In the visible region, hemoglobin is a predominant optical absorber (Fig. 2 C) and has been utilized to study angiogenesis and oxygen metabolism (15,22,29). The absorption spectrum of melanin spans the entire ultraviolet-visible-near-infrared region. As a major pigment in melanosomes (Fig. 2 D) and most melanoma cells (24), melanin is an ideal biomarker for both skin cancer diagnosis and treatment planning. Lipid, absorbing light in

the near-infrared region, is an important component of cell membranes that plays a key role in energy storage and biological signaling. Recent technical advancement in PAM has enabled label-free visualization of lipid-rich intramuscular fat (Fig. 2 E) (30), which holds great potential in lipid biology and atherosclerosis diagnosis. Photoacoustic imaging of several other endogenous chromophores, including water (31), myoglobin (32), and bilirubin (33), has also been documented recently.

If the cellular structure of interest consists of two or more types of chromophores, spectroscopic OR-PAM is often required to differentiate them. For example, fibroblasts contain two major chromophores: cytoplasm and nuclei. Taking advantage of their distinct absorption spectra, OR-PAM is able to distinguish them using two optical

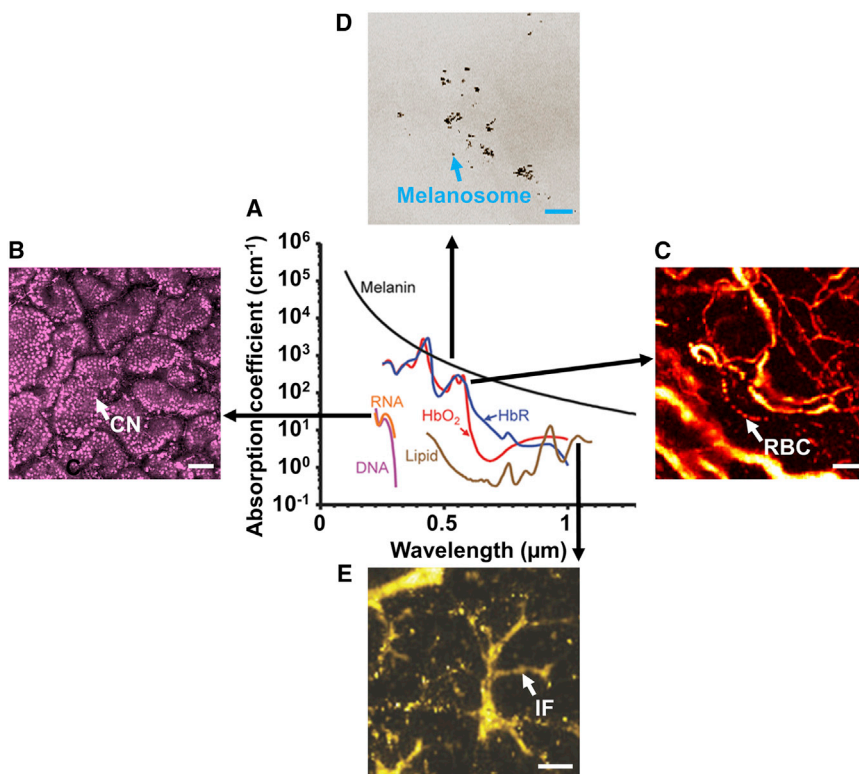


FIGURE 2 (A) Optical absorption spectra of major endogenous chromophores in biological tissues. (Magenta line) DNA, 1 g/L in cell nuclei; (orange line) RNA, 1 g/L in cell nuclei; (red line) HbO_2 , i.e., oxy-hemoglobin, 150 g/L in blood; (blue line) HbR, i.e., deoxy-hemoglobin, 150 g/L in blood; (black line) melanin, 14.3 g/L in human skin medium; (brown line) lipid, 20% vol in tissue. Reproduced from Yao and Wang (50). (B) Ex vivo OR-PAM of epithelial cell nuclei (CN) in a mouse intestinal villi based on the DNA and RNA contrasts. Reproduced from Yao et al. (7). (C) In vivo OR-PAM of red blood cells (RBCs) in mouse ear vasculature based on the hemoglobin contrast. Reproduced from Hu et al. (22). (D) In vivo SW-PAM of melanosomes in a black mouse ear based on the melanin contrast. Reproduced from Zhang et al. (24). (E) Ex vivo acoustic-resolution PAM of a separate intramuscular fat (IF) sample based on the lipid contrast. Reproduced from Li et al. (30). Scale bars: 50 μm in panel B; 50 μm in panel C; 5 μm in panel D; and 1 mm in panel E.

wavelengths: 422 nm for cytoplasm (Fig. 3 A) and 250 nm for nuclei (Fig. 3 B) (34). The superimposed label-free OR-PAM image of fibroblast (Fig. 3 C) matches perfectly the fluorescence image acquired after staining (Fig. 3 D).

If the absorption spectra of the chromophores of interest overlap significantly, spectral decomposition is required. A common example is to differentiate oxy-hemoglobin (HbO₂) and deoxy-hemoglobin (HbR) for the quantification of hemoglobin oxygen saturation (sO₂).

To decompose the experimentally measured blood absorption spectrum, we relate the photoacoustic amplitude of blood (Φ) to the concentrations of HbO₂ and HbR ([HbO₂] and [HbR]) as

$$\Phi(\lambda_i) \propto \mu_a(\lambda_i) \cdot F(\lambda_i) = \{\varepsilon_{\text{HbR}}(\lambda_i) \cdot [\text{HbR}] + \varepsilon_{\text{HbO}_2}(\lambda_i) \cdot [\text{HbO}_2]\} \cdot F(\lambda_i), \quad (1)$$

where λ_i is the optical wavelength; μ_a and F are the blood absorption coefficient and optical fluence, respectively;

and $\varepsilon_{\text{HbO}_2}$ and ε_{HbR} are the molar extinction coefficients of HbO₂ and HbR, respectively (35). By assuming that F is wavelength-independent, which is a valid approximation within the optical diffusion limit in the absence of strong intervening absorption, we can compute [HbO₂] and [HbR] in relative values based on two independent measurements acquired at two wavelengths (λ_1 and λ_2):

$$[\text{HbO}_2] = K \cdot \frac{\Phi(\lambda_1) \cdot \varepsilon_{\text{HbR}}(\lambda_2) - \Phi(\lambda_2) \cdot \varepsilon_{\text{HbR}}(\lambda_1)}{\varepsilon_{\text{HbO}_2}(\lambda_1) \cdot \varepsilon_{\text{HbR}}(\lambda_2) - \varepsilon_{\text{HbO}_2}(\lambda_2) \cdot \varepsilon_{\text{HbR}}(\lambda_1)}, \quad (2)$$

and

$$[\text{HbR}] = K \cdot \frac{\Phi(\lambda_1) \cdot \varepsilon_{\text{HbR}}(\lambda_2) - \Phi(\lambda_2) \cdot \varepsilon_{\text{HbR}}(\lambda_1)}{\varepsilon_{\text{HbR}}(\lambda_1) \cdot \varepsilon_{\text{HbO}_2}(\lambda_2) - \varepsilon_{\text{HbR}}(\lambda_2) \cdot \varepsilon_{\text{HbO}_2}(\lambda_1)}, \quad (3)$$

where K is a constant prefactor.

Consequently, the sO₂ can be computed as

$$s\text{O}_2 = \frac{\Phi(\lambda_1) \cdot \varepsilon_{\text{HbR}}(\lambda_2) - \Phi(\lambda_2) \cdot \varepsilon_{\text{HbR}}(\lambda_1)}{\Phi(\lambda_1) \cdot [\varepsilon_{\text{HbR}}(\lambda_2) - \varepsilon_{\text{HbO}_2}(\lambda_2)] - \Phi(\lambda_2) \cdot [\varepsilon_{\text{HbR}}(\lambda_1) - \varepsilon_{\text{HbO}_2}(\lambda_1)]}. \quad (4)$$

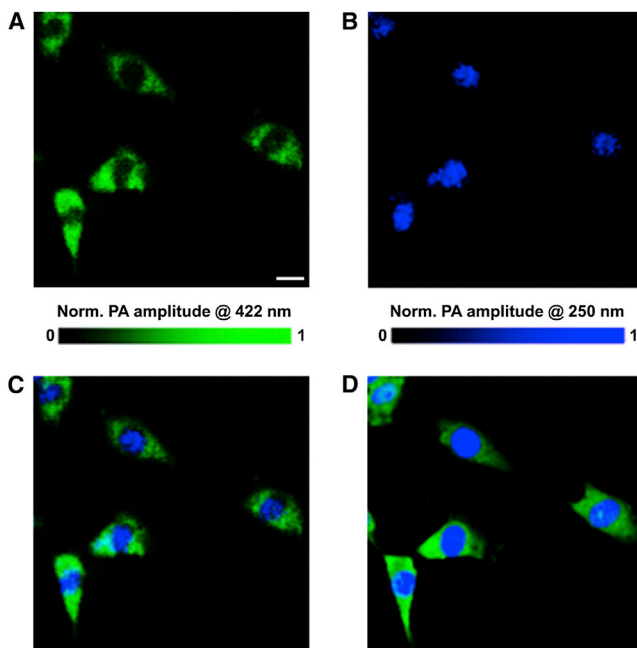


FIGURE 3 Label-free OR-PAM of fixed but unstained fibroblasts at (A) 422 nm and (B) 250 nm. (C) A superimposed image of panels A and B. (D) Fluorescence microscopy of the same sample with mitochondria and nuclei stained in different colors. Scale bar in panel A is 20 μm and applies to all panels. PA, photoacoustic. Reproduced from Zhang et al. (34).

NEW CONTRASTS

Dichroism

Dichroism, or polarization-dependent optical absorption, has been reported recently as a new contrast mechanism for molecular OR-PAM (36). There are three strong motivations to target dichroism:

First, dichroism is a unique molecular signature that provides an ideal specificity.

Second, the polarization-dependent optical absorption enables differential detection, which can eliminate nondichroic background and enhance sensitivity.

Third, and a more specific motivation, is that amyloid plaque, a hallmark of amyloid-associated neurodegenerative diseases, shows linear dichroism when labeled with Congo Red (37).

As a demonstration, OR-PAM examined a brain section from an APP/PS1 Alzheimer's mouse with weak Congo-Red staining (targeting amyloid plaques) and strong Neutral-Red staining (targeting the Golgi apparatus in cells and Nissl granules in neurons, both of which are nondichroic) (Fig. 4, A and B). In both images acquired with two orthogonally polarized optical excitations, the plaque signal was obscured by the overwhelming Neutral Red-stained background (Fig. 4, C and D). Strikingly, whereas

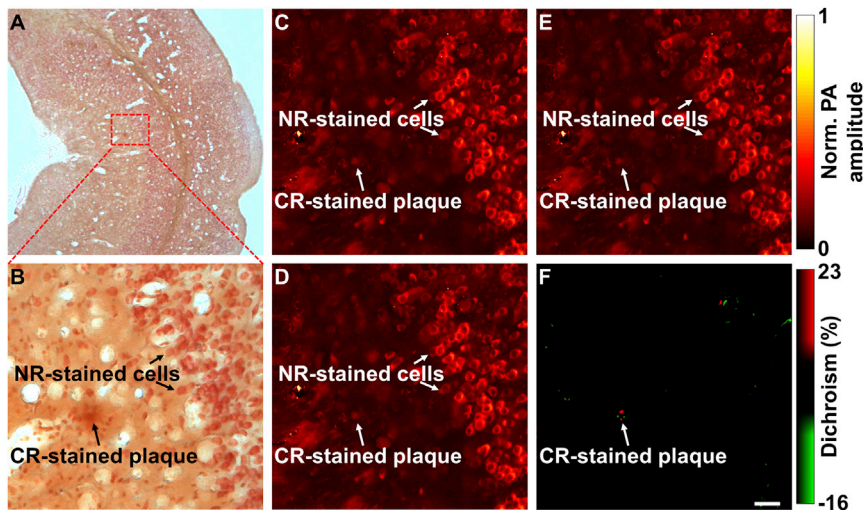


FIGURE 4 Dichroism OR-PAM of amyloid plaques in a brain section from an APP/PS1 mouse. (A) Optical microscopic photo of the brain section double-stained with Congo-Red (CR) and Neutral-Red (NR). (B) Close-up of the boxed area in panel A, showing the CR-stained amyloid plaque and the NR-stained background cells. (C and D) OR-PAM images acquired with each of the two orthogonally polarized optical irradiations. (E and F) Summation and subtraction of panels C and D, respectively. The differential detection in panel F eliminates the NR-stained nondichroic background and highlights the dichroic contrast of the CR-stained amyloid plaque. Scale bar in panel F is 100 μm and applies to all panels. PA, photoacoustic.

summation of the two images (Fig. 4 E) does not reveal new contrast, subtraction completely removed the nondichroic background and highlighted the quadruple-shaped dichroism feature of the amyloid plaque (Fig. 4 F).

Previously, conventional OR-PAM demonstrated intravital amyloid plaque imaging through a cranial window (12). However, such a window may adversely influence the behavior of underlying brain tissues and bias research outcomes (38). Reflection-mode dichroism OR-PAM, with enhanced sensitivity and specificity, may be capable of visualizing individual amyloid plaques through intact skulls and create a powerful *in vivo* screen for anti-amyloid drugs.

Förster resonance energy transfer

The Förster resonance energy transfer (FRET) effect, encoding the distance information between molecules (typically 1–10 nm), has been a valuable tool in biophysical studies of protein interactions and conformational changes (39). OR-PAM has been adopted recently to extend the penetration of high-resolution FRET imaging (40). Unlike conventional FRET microscopy, which relies on the transition of fluorescence energy from donor to acceptor, FRET OR-PAM measures the heat production during the nonradiative dipole-dipole coupling. Therefore, if a nonfluorescent quencher is selected as the acceptor, the FRET energy will be converted into acoustic waves through heat generation and subsequent thermoelastic expansion.

To demonstrate the superior imaging depth of FRET OR-PAM, seven tubes with different concentrations of fluorescent donor Rhodamine 6G (R6G) and nonfluorescent acceptor 1,3'-diethyl-4,2'-quinoloxycarbocyanide iodide (DQOCI) were imaged through freshly harvested mouse skin (Fig. 5 A). The strong optical scattering of the skin severely degrades the resolution of the fluorescence FRET image and overwhelms the quenching effect of the donor (Fig. 5 B). In contrast, OR-PAM clearly resolves all seven

tubes (Fig. 5 C) and provides sufficient signal/noise for the quantification of FRET efficiency (40). Further, the cross-sectional (B-scan) FRET OR-PAM image validates an extended imaging depth of ~ 1 mm (Fig. 5 D).

PHOTOACOUSTIC FLOWOXIGRAPHY: A NEW FRONTIER OF OR-PAM

Integrating the fine length- and timescales, OR-PAM opens the door to understanding the fundamental mechanism of oxygen metabolism in biological systems. Photoacoustic flowoxigraphy, a new OR-PAM implementation, has demonstrated real-time multiparameter quantification of oxygen release from single red blood cells (RBCs) *in vivo* (29).

Near video-rate (20 Hz) dual-wavelength B-scan monitoring of a mouse-brain capillary *in vivo* clearly shows that the hemoglobin in a representative RBC is deoxygenated by 3% over a 32- μm travel distance (Fig. 6 A). Taking advantage of the ultra-short-wavelength switching time (20 μs), fast scanning speed, and high spatial resolution, multiple hemodynamic parameters—including the concentration of total hemoglobin (HbT), $s\text{O}_2$, $s\text{O}_2$ reduction per unit length ($\nabla s\text{O}_2$), and flow speed (v_f)—can be simultaneously quantified at the single-RBC level (Fig. 6 B). Further, the rate of single-RBC oxygen release ($r\text{O}_2$) can be defined and computed in relative values as

$$r\text{O}_2 \propto \frac{\text{HbT} \cdot (s\text{O}_{2\text{in}} - s\text{O}_{2\text{out}})}{t} = \text{HbT} \cdot \nabla s\text{O}_2 \cdot v_f, \quad (5)$$

where $s\text{O}_{2\text{in}}$ and $s\text{O}_{2\text{out}}$ are the $s\text{O}_2$ values of the RBC when entering and exiting the region of interest, respectively.

Photoacoustic flowoxigraphy experimentally shows that $r\text{O}_2$ is proportional to the total amount of oxygen released by the RBC ($\nabla s\text{O}_2$ multiplied by the pathlength), but inversely proportional to its dwell time in the field of view

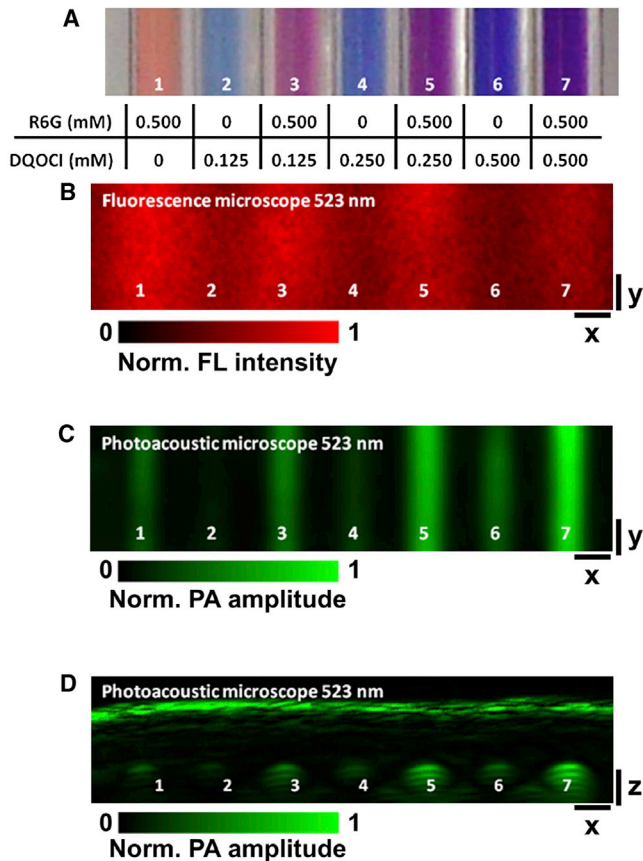


FIGURE 5 (A) Photograph of the tube phantom and tabulation of the donor (R6G) and acceptor (DQOCI) concentrations. (B) Fluorescence microscopy and (C) OR-PAM of the same tube phantom with overlaid mouse skin tissue at 523 nm. (D) B-scan OR-PAM image of the tubes acquired at 523 nm. Scale bars: 500 μm . FL, fluorescence. PA, photoacoustic. Reproduced from Wang and Wang (40).

(pathlength divided by v_f) (Fig. 6 C). The result suggests two possible underlying mechanisms for the upregulation of local oxygen metabolism at the cellular level:

1. Increase in v_f allows more RBCs to flow through the tissue region within a given time period; and
2. More oxygen is extracted from individual RBCs, if v_f is restricted.

OUTLOOK: TRANSLATIONAL POTENTIAL OF OR-PAM TO CLINIC

Early detection of microvascular complications in diabetes

Diabetic microvascular complications are often asymptomatic during their early stages, and may become irreversible once symptoms develop (41). Label-free multiparameter OR-PAM of the microcirculation in vivo at high spatiotemporal resolution provides a comprehensive means for early detection of microvascular morbidity in diabetes (42).

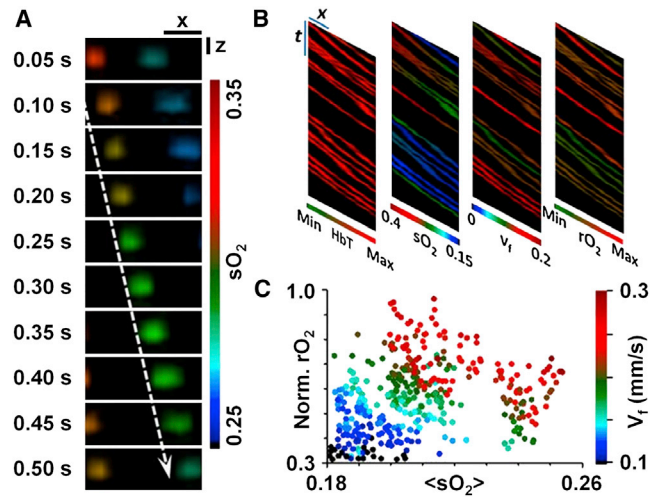


FIGURE 6 (A) Sequential snapshots of single RBCs releasing oxygen in a living mouse brain. Scale bars: 10 μm along the x direction and 30 μm along the z direction. Blood flows from left to right. (Dashed arrow) Trajectory of a single flowing RBC. (B) Simultaneous multiparameter OR-PAM of single RBCs in vivo, showing total hemoglobin concentration (HbT), sO_2 , flow speed (v_f), and relative oxygen release rate (rO_2). At each time point, the one-dimensional profile along the x axis shows the maximum amplitude projection along the depth direction. Each oblique line in the x - t images tracks one RBC. Scale bars are 10 μm and 1 s along the x axis and t axis, respectively. (C) Normalized rO_2 versus ∇sO_2 at varied v_f . Reproduced from Wang et al. (29).

To translate this technology to the clinic, exciting progress has been made very recently. The microvascular anatomy of a label-free human finger cuticle (Fig. 7 A) was visualized in vivo using the second-generation OR-PAM (22), which enables fiber-based instrument scanning with enhanced detection sensitivity compared with the first-generation system (6). Individual capillary loops were clearly resolved. With a dual-wavelength measurement and spectral decomposition, the blood oxygenation level within individual cuticle microvessels was further revealed (Fig. 7 B). The high spatial resolution of OR-PAM allows us to observe the sharp transition in sO_2 at the tip of a representative capillary loop, which indicates a marked oxygen release from blood hemoglobin (Fig. 7 C).

Integrating other hemodynamic parameters—including blood flow, oxygen metabolism, and pulse-wave velocity (43)—into second-generation OR-PAM would lead to a promising tool for the clinical diagnosis of microvascular complications in early-stage diabetes.

Tumor metastasis

Melanoma is malignant skin cancer with a high propensity for metastasis (44). Circulating melanoma cells (CMCs) have been regarded as a potential predictor for metastasis (45). However, blood-test-based ex vivo detection methods require a minimum number of 5000–25,000 CMCs in the

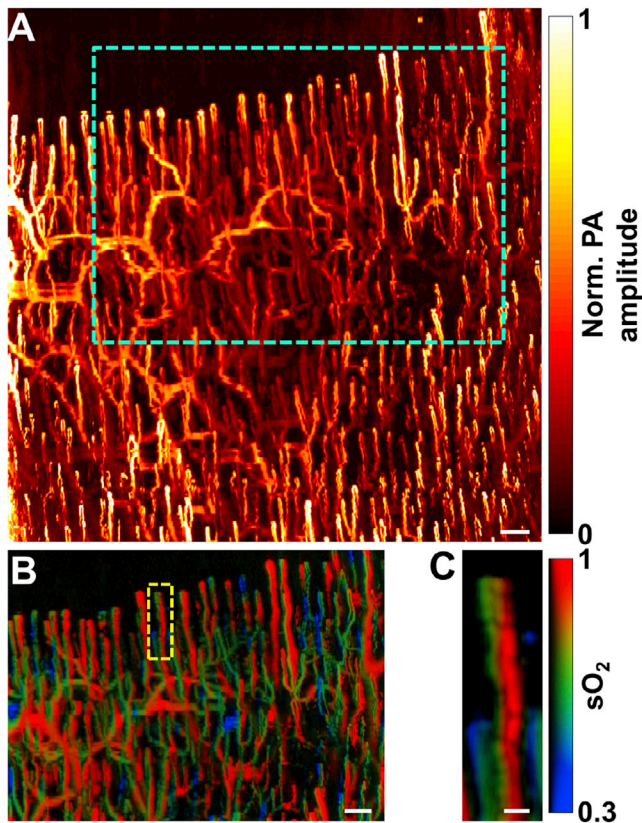


FIGURE 7 Label-free OR-PAM of (A) microvascular anatomy and (B) oxygen saturation of hemoglobin in human finger cuticle in vivo. (C) Close-up of the capillary loop indicated in B. PA, photoacoustic. Scale bars: 200 μm in (A) and (B), and 50 μm in (C).

blood stream, which likely corresponds to a late stage of metastasis (46).

Taking advantage of the strong optical absorption of melanin, OR-PAM holds great potential in detecting CMCs in vivo. As a proof-of-principle experiment, OR-PAM was used to monitor melanoma cells circulating in a glass microtube along with bovine blood at a concentration of $4 \times 10^6/\text{mL}$ (47). The near-infrared wavelength of 1064 nm was chosen to minimize the influence of blood absorption. Similar to photoacoustic flow cytometry (48), the laser beam was focused and kept stationary at the center of the tube. CMCs passing through the optical focal zone were excited, and the generated photoacoustic signals were detected with an ultrasonic transducer. Individual melanoma cells were clearly observed with a mean signal/background of 4:1 (Fig. 8 A), and the CMC flow speed was estimated to be 1.6–3.1 mm/s (Fig. 8 B) using motion mode (M-mode) photoacoustic flow imaging (49).

Photoacoustic flowoxigraphy possesses adequate spatial and temporal resolutions for in vivo real-time CMC imaging and would enable in-depth study of the size distribution, clustering, self-seeding, and extravasation of CMCs. Operating at three optical wavelengths (two visible wavelengths for the quantification of oxygen metabolism and one near-

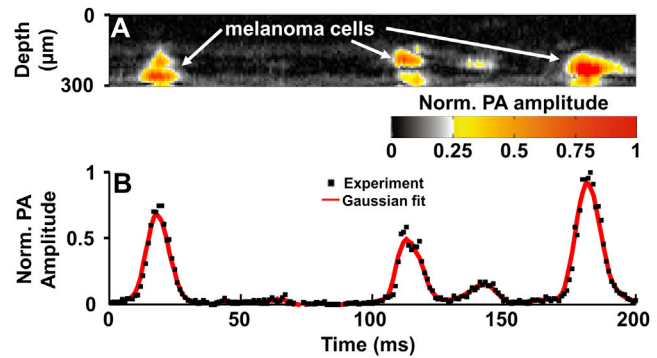


FIGURE 8 Label-free OR-PAM of melanoma cells flowing with bovine blood through a microtube. (A) M-mode PAM image tracks three melanoma cells. (B) Time course of the photoacoustic amplitude shows the transverse profile of the cells. PA, photoacoustic. Reproduced from Wang et al. (47).

infrared wavelength for CMC detection), photoacoustic flowoxigraphy holds the potential to unveil the relationship between CMCs and tumor progression in patients.

This work was sponsored in part by National Institutes of Health grant Nos. R01 EB008085, R01 CA134539, U54 CA136398, R01 CA157277, R01 CA159959, and DP1 EB016986 (National Institutes of Health Director's Pioneer Award). Lihong V. Wang has a financial interest in Microphotoacoustics Inc., and Endra Inc., which, however, did not support this work.

REFERENCES

- White, J. G., W. B. Amos, and M. Fordham. 1987. An evaluation of confocal versus conventional imaging of biological structures by fluorescence light microscopy. *J. Cell Biol.* 105:41–48.
- Denk, W., J. H. Strickler, and W. W. Webb. 1990. Two-photon laser scanning fluorescence microscopy. *Science.* 248:73–76.
- Itzkan, I., L. Qiu, ..., L. T. Perelman. 2007. Confocal light absorption and scattering spectroscopic microscopy monitors organelles in live cells with no exogenous labels. *Proc. Natl. Acad. Sci. USA.* 104:17255–17260.
- Huang, D., E. A. Swanson, ..., J. G. Fujimoto. 1991. Optical coherence tomography. *Science.* 254:1178–1181.
- Freudiger, C. W., W. Min, ..., X. S. Xie. 2008. Label-free biomedical imaging with high sensitivity by stimulated Raman scattering microscopy. *Science.* 322:1857–1861.
- Maslov, K., H. F. Zhang, ..., L. V. Wang. 2008. Optical-resolution photoacoustic microscopy for in vivo imaging of single capillaries. *Opt. Lett.* 33:929–931.
- Yao, D. K., K. Maslov, ..., L. V. Wang. 2010. In vivo label-free photoacoustic microscopy of cell nuclei by excitation of DNA and RNA. *Opt. Lett.* 35:4139–4141.
- Hu, S., K. Maslov, ..., L. V. Wang. 2009. Functional transcranial brain imaging by optical-resolution photoacoustic microscopy. *J. Biomed. Opt.* 14:040503.
- Shi, W., P. Shao, ..., R. J. Zemp. 2013. In vivo dynamic process imaging using real-time optical-resolution photoacoustic microscopy. *J. Biomed. Opt.* 18:26001.
- Yao, J., K. I. Maslov, ..., L. V. Wang. 2011. Label-free oxygen-metabolic photoacoustic microscopy in vivo. *J. Biomed. Opt.* 16:076003.
- Liu, T., Q. Wei, ..., H. F. Zhang. 2011. Combined photoacoustic microscopy and optical coherence tomography can measure metabolic rate of oxygen. *Biomed. Opt. Express.* 2:1359–1365.

12. Hu, S., P. Yan, ..., L. V. Wang. 2009. Intravital imaging of amyloid plaques in a transgenic mouse model using optical-resolution photoacoustic microscopy. *Opt. Lett.* 34:3899–3901.
13. Cai, X., L. Li, ..., L. V. Wang. 2012. Multi-scale molecular photoacoustic tomography of gene expression. *PLoS ONE*. 7:e43999.
14. Tsytsarev, V., S. Hu, ..., L. V. Wang. 2011. Photoacoustic microscopy of microvascular responses to cortical electrical stimulation. *J. Biomed. Opt.* 16:076002.
15. Oladipupo, S., S. Hu, ..., J. M. Arbeit. 2011. VEGF is essential for hypoxia-inducible factor-mediated neovascularization but dispensable for endothelial sprouting. *Proc. Natl. Acad. Sci. USA*. 108:13264–13269.
16. Oladipupo, S., S. Hu, ..., J. M. Arbeit. 2011. Conditional HIF-1 induction produces multistage neovascularization with stage-specific sensitivity to VEGFR inhibitors and myeloid cell independence. *Blood*. 117:4142–4153.
17. Favazza, C. P., S. Hu, ..., L. V. Wang. 2011. In vivo multiscale photoacoustic microscopy of human skin. *Proc. SPIE*. 7899:789946.
18. Hu, S., B. Rao, ..., L. V. Wang. 2010. Label-free photoacoustic ophthalmic angiography. *Opt. Lett.* 35:1–3.
19. Jiao, S., M. Jiang, ..., H. F. Zhang. 2010. Photoacoustic ophthalmoscopy for in vivo retinal imaging. *Opt. Express*. 18:3967–3972.
20. Cai, X., B. S. Paratala, ..., L. V. Wang. 2012. Multiscale photoacoustic microscopy of single-walled carbon nanotube-incorporated tissue engineering scaffolds. *Tissue Eng. Part C Methods*. 18:310–317.
21. Wang, L. V., and S. Hu. 2012. Photoacoustic tomography: in vivo imaging from organelles to organs. *Science*. 335:1458–1462.
22. Hu, S., K. Maslov, and L. V. Wang. 2011. Second-generation optical-resolution photoacoustic microscopy with improved sensitivity and speed. *Opt. Lett.* 36:1134–1136.
23. Zhang, C., K. Maslov, ..., L. V. Wang. 2012. Reflection-mode submicron-resolution in vivo photoacoustic microscopy. *J. Biomed. Opt.* 17:020501.
24. Zhang, C., K. Maslov, and L. V. Wang. 2010. Subwavelength-resolution label-free photoacoustic microscopy of optical absorption in vivo. *Opt. Lett.* 35:3195–3197.
25. Zhang, H. F., K. Maslov, ..., L. V. Wang. 2006. Functional photoacoustic microscopy for high-resolution and noninvasive in vivo imaging. *Nat. Biotechnol.* 24:848–851.
26. Kinsler, L. E. 2000. *Fundamentals of Acoustics*. Wiley, New York.
27. Brekhovskikh, L. M. 1980. *Waves in Layered Media*. Academic Press, New York.
28. Reference deleted in proof.
29. Wang, L., K. Maslov, and L. V. Wang. 2013. Single-cell label-free photoacoustic flowoxigraphy in vivo. *Proc. Natl. Acad. Sci. USA*. 110:5759–5764.
30. Li, R., M. N. Slipchenko, ..., J.-X. Cheng. 2013. Compact high power barium nitrite crystal-based Raman laser at 1197 nm for photoacoustic imaging of fat. *J. Biomed. Opt.* 18:040502.
31. Xu, Z., Q. Zhu, and L. V. Wang. 2011. In vivo photoacoustic tomography of mouse cerebral edema induced by cold injury. *J. Biomed. Opt.* 16:066020.
32. Zhang, C., Y. J. Cheng, ..., L. V. Wang. 2012. Label-free photoacoustic microscopy of myocardial sheet architecture. *J. Biomed. Opt.* 17:060506.
33. Zhou, Y., C. Zhang, ..., L. V. Wang. 2012. Photoacoustic microscopy of bilirubin in tissue phantoms. *J. Biomed. Opt.* 17:126019.
34. Zhang, C., Y. S. Zhang, ..., L. V. Wang. 2013. Label-free photoacoustic microscopy of cytochromes. *J. Biomed. Opt.* 18:20504.
35. Zhang, H. F., K. Maslov, ..., L. V. Wang. 2007. Imaging of hemoglobin oxygen saturation variations in single vessels in vivo using photoacoustic microscopy. *Appl. Phys. Lett.* 90:3.
36. Hu, S., K. M., P. Yan, ..., L. V. Wang. 2012. Dichroism optical-resolution photoacoustic microscopy. In *Biomedical Optics and 3-D Imaging* Optical Society of America, Miami, FL BM2B.8.
37. Jin, L. W., K. A. Claborn, ..., B. Kahr. 2003. Imaging linear birefringence and dichroism in cerebral amyloid pathologies. *Proc. Natl. Acad. Sci. USA*. 100:15294–15298.
38. Yan, P., A. W. Bero, ..., J. M. Lee. 2009. Characterizing the appearance and growth of amyloid plaques in APP/PS1 mice. *J. Neurosci.* 29:10706–10714.
39. Periasamy, A., S. S. Vogel, and R. M. Clegg. 2012. FRET 65: a celebration of Förster. *J. Biomed. Opt.* 17:011001.
40. Wang, Y., and L. V. Wang. 2012. Förster resonance energy transfer photoacoustic microscopy. *J. Biomed. Opt.* 17:086007.
41. Marcovecchio, M. L., P. H. Tossavainen, and D. B. Dunger. 2010. Prevention and treatment of microvascular disease in childhood type 1 diabetes. *Br. Med. Bull.* 94:145–164.
42. Krumholz, A., L. Wang, ..., L. V. Wang. 2012. Functional photoacoustic microscopy of diabetic vasculature. *J. Biomed. Opt.* 17:060502.
43. Yeh, C., S. Hu, ..., L. V. Wang. 2012. Photoacoustic microscopy of blood pulse wave. *J. Biomed. Opt.* 17:070504.
44. Cummins, D. L., J. M. Cummins, ..., A. Chanmugam. 2006. Cutaneous malignant melanoma. *Mayo Clin. Proc.* 81:500–507.
45. Hu, X., C. W. Wei, ..., X. Gao. 2013. Trapping and photoacoustic detection of CTCs at the single cell per milliliter level with magneto-optical coupled nanoparticles. *Small*. 9:2046–2052.
46. Nedosekin, D. A., M. Sarimollaoglu, ..., V. P. Zharov. 2011. In vivo ultra-fast photoacoustic flow cytometry of circulating human melanoma cells using near-infrared high-pulse rate lasers. *Cytometry A*. 79:825–833.
47. Wang, Y., K. Maslov, ..., L. V. Wang. 2011. Fiber-laser-based photoacoustic microscopy and melanoma cell detection. *J. Biomed. Opt.* 16:011014.
48. Zharov, V. P., E. I. Galanzha, ..., V. V. Tuchin. 2006. In vivo photoacoustic flow cytometry for monitoring of circulating single cancer cells and contrast agents. *Opt. Lett.* 31:3623–3625.
49. Fang, H., and L. V. Wang. 2009. M-mode photoacoustic particle flow imaging. *Opt. Lett.* 34:671–673.
50. Yao, J., and L. V. Wang. 2013. Photoacoustic microscopy. *Laser Photon Rev.* 31 Jan. 2013. <http://dx.doi.org/10.1002/lpor.201200060>.